RSC Advances

This is an *Accepted Manuscript*, which has been through the Royal Society of Chemistry peer review process and has been accepted for publication.

Accepted Manuscripts are published online shortly after acceptance, before technical editing, formatting and proof reading. Using this free service, authors can make their results available to the community, in citable form, before we publish the edited article. This *Accepted Manuscript* will be replaced by the edited, formatted and paginated article as soon as this is available.

You can find more information about *Accepted Manuscripts* in the **Information for Authors**.

Please note that technical editing may introduce minor changes to the text and/or graphics, which may alter content. The journal's standard **Terms & Conditions** and the **Ethical guidelines** still apply. In no event shall the Royal Society of Chemistry be held responsible for any errors or omissions in this *Accepted Manuscript* or any consequences arising from the use of any information it contains.

The Effect of Silica Sols on Electrodeposited Zinc Coatings for Sintered NdFeB

Rui Cao, Liqun Zhu, Huicong Liu, Wei Yang, Weiping Li *

Key Laboratory of Aerospace Materials and Performance (Ministry of Education), School of Materials Science and Engineering, Beihang University, Beijing 100191, China

ABSTRACT

We developed an in situ method to prepare silica particles contained zinc coatings on NdFeB. Silica sols with silica nanoparticles of 30–150 nm in diameter were prepared through the hydrolysis and condensation of tetraethyl orthosilicate with an acid catalyst. Zinc coatings were prepared on NdFeB magnets using plating baths that contained the silica sols. The effect of the volume content of silica sols on the zinc coatings was studied via scanning electron microscopy (SEM), X-Ray diffraction (XRD) and electrochemical analysis. The SEM results showed that silica nanoparticles were embedded in the zinc particles. Compared with the zinc coatings that were electroplated in the other plating baths, the surface morphology of the zinc coating formed when the silica sol content in the plating bath was in proper range exhibited better uniformity. The decrease in the corrosion current density value and the increase in the impedance value that were measured via electrochemical testing demonstrated that the embedded silica nanoparticles, which

served as corrosion inhibitors, improved the corrosion resistance capability of the zinc coatings on

the NdFeB magnets.

1. INTRODUCTION

Sintered NdFeB permanent magnets have been widely used for many applications in various fields, such as electronics, acoustics, communications, automation, magnetic resonance imaging, and biomedical applications, by virtue of their excellent magnetic properties.[1, 2] However, their multiphase microstructure, which improves their magnetic properties, also makes NdFeB magnets vulnerable to corrosion. There are two types of protective coatings that can be applied to sintered NdFeB magnets: cathodic and anodic coatings.[3-8] A cathodic coating protects the sintered NdFeB magnet by segregating the substrate from the corrosive medium. Once the cathodic coating is ruptured and the sintered NdFeB is exposed to the corrosive medium, a large cathodic coupling forms with a small NdFeB anode, which can accelerate the corrosion of the sintered NdFeB magnet. An anodic coating insulates the substrate from the corrosive medium. Even when the anodic coating is damaged and the NdFeB is exposed to the corrosive medium, the anodic coating may act as a sacrificial anode and slow the corrosion of the metal substrate.[9] The role of an anodic coating in corrosion protection is a combination of mechanical isolation and electrochemical protection. Zinc coatings have been widely used as anodic coatings for NdFeB magnets because of their low cost and ready adaptability to mass production.[2]

To improve the corrosion resistance of zinc coatings, various strategies focused on combining zinc with other particles or corrosion inhibitors have been proposed over the past few years.[10-15] Silica and silicate materials have been shown to possess anti-corrosive properties.[16-20] A composite coating of zinc and silica is an effective means of improving the properties of zinc coatings.[21, 22]

Zinc and silica composite coatings can be prepared from silicate solutions or silica sols by dipping, spinning and electroplating silica films on top of zinc coatings.[2, 23, 24] It is also possible to obtain zinc and silica composite coatings from silica nanoparticles or a silicon-containing zinc solution using electroplating or sintering methods.[25-29] Electrodeposition was an effective method to obtain silica contained zinc coating with better protection performance on steel substrates.[30] The silica particles, which become embedded in the zinc coating, contribute to the dimensional stabilization of the protective zinc layer.[13]

Acid-catalyzed silica sols tend to form linear chains, which can be catalyzed to form silica nanoparticles by hydroxyl groups, and the cathodic electroplating process promotes the agglomeration and adsorption of these silica chains on the electrode surface.[31-33] Therefore, it is possible to control the migration and deposition of the silica particles on the surface of the cathode during the electrodeposition of the zinc coating.[34-39]

In this work, we demonstrated a one-step in situ method for successfully preparing a uniform silica-containing zinc coating on the surface of an NdFeB magnet via electrodeposition by introducing silica sols into the plating bath. The content of silica sols in the plating bath was varied to investigate the effect of the silica sols on the electrodeposited zinc coatings. The sol-gel process of the acidic silica sols was promoted by the cathodic deposition reaction, leading to the generation of embedded silica nanoparticles. As observed from the morphologies of the zinc coatings formed from the silica-sol-containing plating baths, the crystal size and distribution of the zinc particles were notably affected by the addition of silica sols. We also observed the distributions of silica

throughout the zinc coatings and the different shapes of the silica nanoparticles between the zinc

grain boundaries as the silica sol content in the plating baths increased. The silica nanoparticles

embedded in the zinc coatings were found to improve the corrosion resistance of the zinc coatings.

Additionally, it was demonstrated that silica sols are an effective additive during the

electrodeposition reaction to enhance the uniformity of the zinc coating.

2. EXPERIMENTAL SECTION

2.1 Materials Powder-sintered. NdFeB magnets (Jingci Magnet Co, China) of grade 42H

($Nd_{10.1}Tb3.1Fe_{77.4}B_{9.4}$) were used as substrates for the deposition of zinc coatings in

silica-sol-containing plating baths. Tetraethyl orthosilicate (TEOS, kermel, highly pure, China),

ethyl alcohol (EtOH, 99.7%), zinc chloride ($ZnCl_2$, 98%), potassium chloride (KCl, 99.5%) and

HCl (11.9 mol/L) were used as received without any further purification.

2.2 Synthesis of the silica sols. Silica sols were prepared via the acid-catalyzed reaction of

tetraethyl orthosilicate. In the synthesis procedure, TEOS and ethanol were added to a mixture of

deionized water, acid catalyst and ethanol, followed by stirring at (30 ± 1) °C for 24 h using a

magnetic stirrer (RT5, IKA) at the speed of 240 rpm. The pH value of the mixture was adjusted to

4.6 through the addition of 1 mol/L HCl solution, which served as the acid catalyst and stabilizer.

The mixtures were aged at (30 ± 1) °C for another 24 h.

2.3 Electrodeposition. For the electrodeposition process, the silica sols were added to acid zinc

plating baths ($ZnCl_2$ 70 g/L, KCl 200 g/L). Silica sols were uniformly dispersed under stirring at

(25 ± 1) °C for 10 min using RT5 at the speed of 300 rpm. The volume fraction of silica sols in each

plating bath varied from 0 to 25%; specifically, contents of 0, 5, 15 and 25% were tested. The pH

of all plating bath was adjusted to 4.5 before electrodeposition. The substrate material consisted of

well-cleaned NdFeB magnets. The electrodeposition process was conducted at a current density of

1.2 A/dm^2 at room temperature.

2.4 Characterization. The particle distributions and surface roughnesses of the zinc coatings

were investigated using field emission scanning electron microscopy (FESEM, JSM 7500). X-ray

diffraction (XRD) analysis was performed using a Rigaku D/MAX-RB with Cu K radiation

(K=0.15406 nm), which was used to analyze the zinc grain growth. The zeta potential of the silica

particles was calculated using an electrophoretic light scattering spectrometer (Zeta Sizer, Model

3000HS, Molvern instrument Ltd.). A CHI604A electrochemical workstation was used to perform

electrochemical dynamic polarization and electrochemical impedance spectroscopy (EIS) in 3.5

wt.% NaCl solution at room temperature. The tests were performed using a standard

three-electrode system with a platinum foil and a saturated calomel electrode as the counter and

reference electrodes, respectively. The polarization measurements were carried out with a

scanning rate of 1 mV/s. Electrochemical impedance spectroscopy data were obtained under

potentiostatic control with a signal amplitude of 5 mV in the frequency range of 10^5 Hz to 1 mHz.

The samples were stabilized in 3.5 wt.% NaCl solution for 30minutes before EIS tests to ensure

potential stability, and open circuit potential was used as initial potential. The electrochemical tests

were performed at least three times to ensure the reproducibility of the results.

3. RESULTS AND DISCUSSION

Figure 1 shows several representative low-magnification SEM images of the zinc coatings formed from the silica-sol-containing plating baths (SSPBs) on the NdFeB magnet samples. It is evident that the silica sols significantly modified the size and distribution of the zinc particles via the adsorption effect. As shown in Figure 1 (A), the surface of the zinc coating produced from the silica-sol-free plating bath was very heterogeneous, and with a broad size distribution of the zinc particles. When the zinc was deposited without silica sols, the quantity of nucleation points was lower, and the particle size was larger. The zinc particles aggregated on the substrate, and the grain boundaries of the zinc particles were remarkable. Figure 1 (B) shows the surface of the zinc coating obtained from the 5% SSPB, from which it is evident that the zinc particle size decreased considerably with the addition of silica sols. It was observed that the adsorption of silica sols limited the growth process of the zinc particles and generated more nucleation sites than were observed in the sample shown in (A). The inset to Figure 1 (B) shows that some silica particles aggregated and adsorbed on the surfaces of the zinc particles as well as at the grain boundaries. Figure 1 (C) shows the surface of the zinc coating obtained from the 15% SSPB. The zinc particle size was further reduced in comparison with (A) and (B), and the zinc coating evenly covered the NdFeB substrate. There was no zinc grain with obvious geometric outline on the surface. Several silica sol particles were present on the surfaces of the zinc particles, and several embedded silica inclusions were distributed between the zinc grain boundaries. The inset shows that the adsorbed silica sols caused the formation of more nucleation sites and changed the crystallization direction

of the zinc particles, which became extruded before they could grow to form typical hexagonal particles. In addition, the adsorbed silica nanoparticles could become wrapped with the deposited coating during the growth process of the zinc particles. When the silica sol content reached 25%, as shown in Figure 1 (D), the zinc particle size was further reduced. The silica particles that were adsorbed at the zinc grain boundaries were more visible, as seen from the inset to Figure 1 (D). Thus, as the silica sol content was increased from 0 to 25%, the silica nanoparticles became more uniformly distributed on the surface, whereas the agglomeration size of the silica decreased. The amount of adsorbed silica nanoparticles that were embedded in the zinc grains also varied. At the same time, the size, number and crystallization direction of the zinc particles were also significantly affected by the increase in the silica sol content.
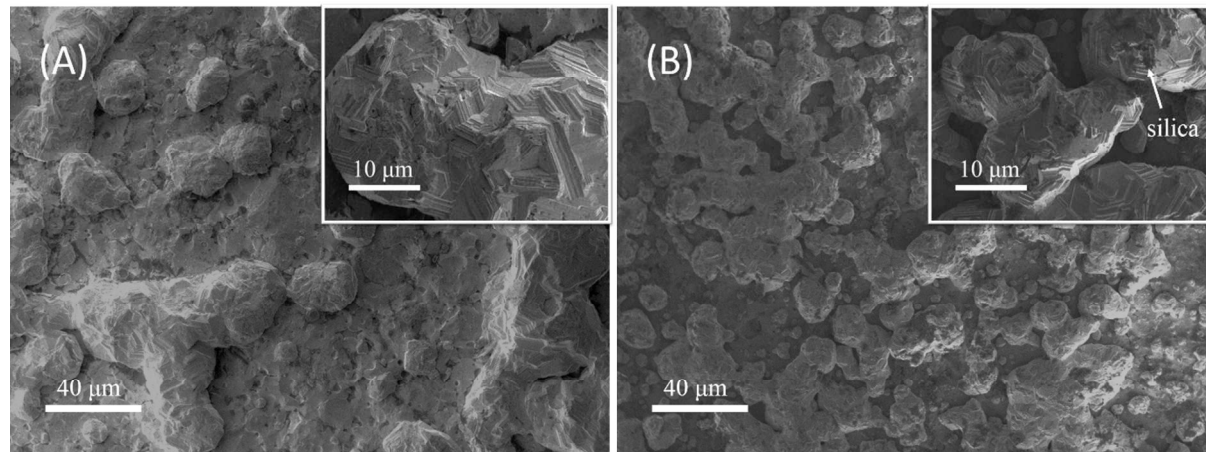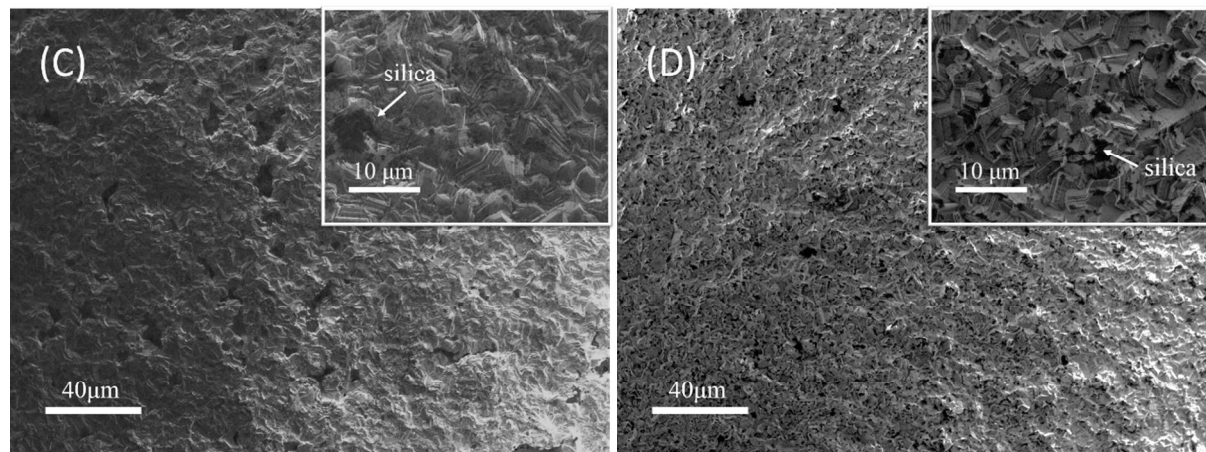
Figure 1. Representative SEM images of (A) the zinc coating obtained from the 0% SSPB, (B) the zinc coating obtained from the 5% SSPB, (C) the zinc coating obtained from the 15% SSPB, and (D) the zinc coating obtained from the 25% SSPB. The insets are the corresponding high-resolution images.

Figures 2 (A) (B) (C) (D) show representative microstructural features of the zinc particles and grain boundaries in the zinc coatings formed from plating baths with silica sol contents of 0, 5, 15 and 25%, respectively. As shown in Figure 2 (A), there were no silica nanoparticles at the zinc grain boundaries in the coating formed from the 0% SSPB. The zinc particles followed the crew dislocation growth mechanism, forming hexagonal grains. Figure 2 (B) shows the zinc coating grain boundaries in the coating formed from the 5% SSPB. Some silica agglomerates were adsorbed at the zinc grain boundaries. As shown in Figure 2 (C), in the coating formed from the 15% SSPB, the silica particles adsorbed on the zinc grains and filled the gaps between zinc particles. There were also some visible silica nanoparticles embedded in the zinc grains. Figure 2 (D) shows that compared with the samples at lower silica sol contents, the agglomeration size of the adsorbed

silica decreased in the coating formed from the 25% SSPB. This image also shows several silica nanoparticles with diameters below 100 nm, which were evenly adsorbed on the crystal plane of the zinc grains. Moreover, from Figure 2, it is clear that the crystal orientation of the zinc grains gradually changed with the increase in the silica sol content.
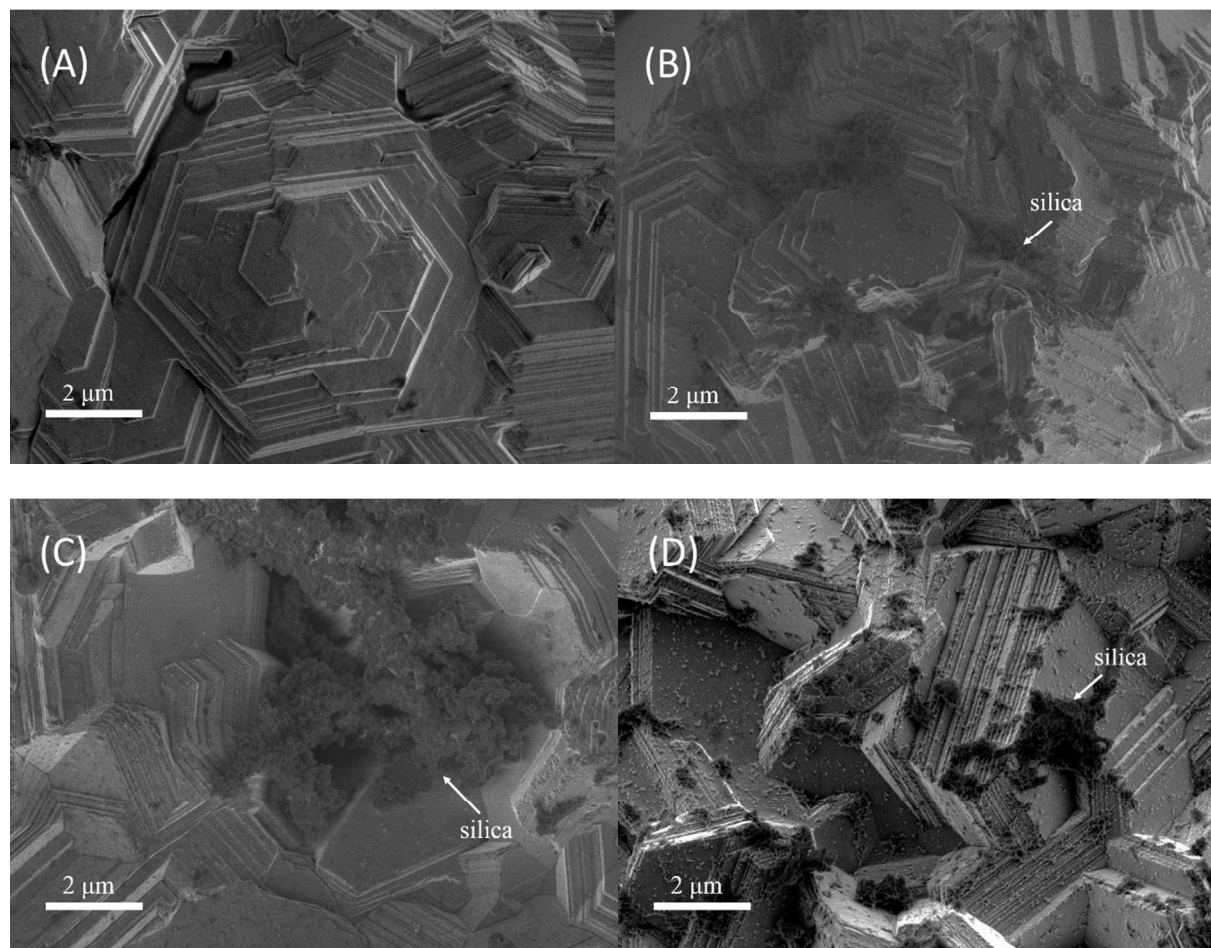
Figure 2. Representative SEM images of zinc grain boundaries in (A) the zinc coating obtained from the 0% SSPB, (B) the zinc coating obtained from the 5% SSPB, (C) the zinc coating obtained from the 15% SSPB, and (D) the zinc coating obtained from the 25% SSPB.

As shown in Figure 3, energy dispersive spectrometry (EDS) analyses were conducted to

RSC Advances

evaluate the distribution of the silica phase. Figure 3 (A) shows that in the coating produced from the 5% SSPB, some portions of the zinc grain boundaries were covered by aggregated silica nanoparticles. However, the distribution of the silica phase was not uniform, and several zinc grain boundaries lacked coverage by silica nanoparticles. As shown in Figure 3 (B), when the silica sol content of the SSPB reached 15%, more silica nanoparticles aggregated at the zinc grain boundaries, and the silica phase almost completely covered the zinc grains. Figure 3 (C) shows the zinc coating obtained from the 25% SSPB. The silica phase was uniformly adsorbed on this zinc coating. In the electrodeposition process, the electric charge tended to accumulate more on the zinc grain boundaries. For this reason, the strength of the electric field on the grain boundaries are stronger than that on the grain surfaces. The hydroxyl rich silica particles are more likely to aggregate at the boundaries of zinc grains. Because the outline of the silica phase distribution was more likely to form a hexagon, which is the typical geometrical shape of zinc grains, it was concluded that the silica nanoparticles were more likely to aggregate at the zinc grain boundaries in this case.
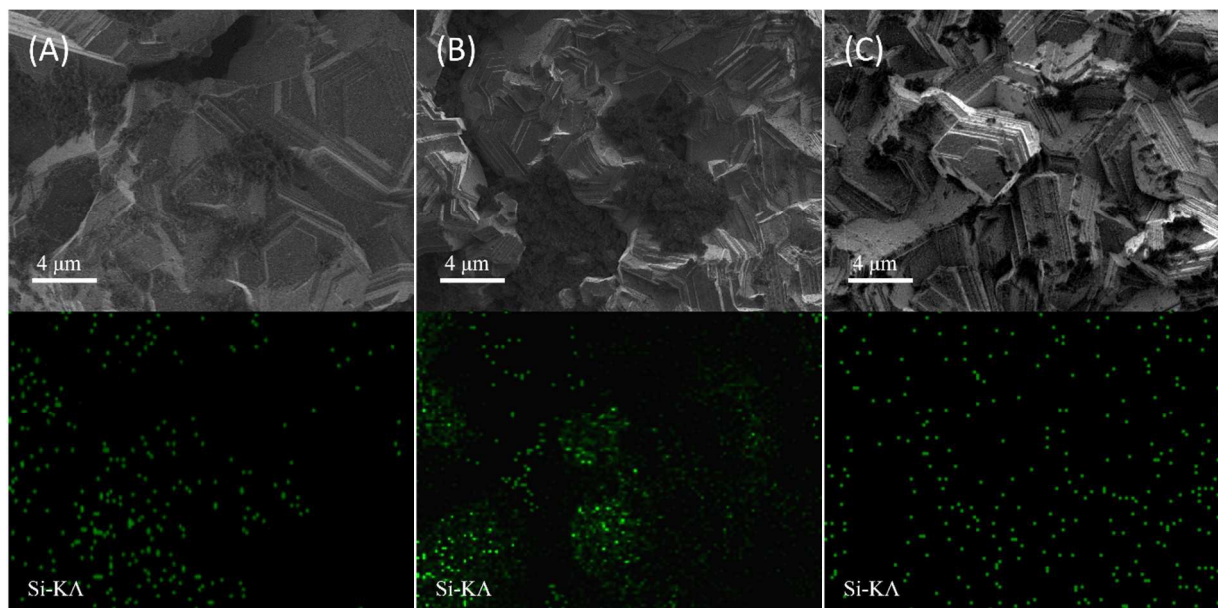
Figure 3 EDS analyses of zinc coatings obtained from (A) the 5% SSPB, (B) the 15% SSPB, and (C) the 25% SSPB.

Figures 4 (A) (B) (C) (D) show the cross sections of the zinc coatings formed in plating baths with various silica sol contents. To distinguish the substrates from the zinc coatings, the polished specimens were etched with ammonia and then ultrasonically cleaned in alcohol. The spectra of liner EDS analyses, which scanned following the yellow arrows in SEM images, shows the distribution of different elements. Figure 4 (A) shows the zinc coating obtained from the 0% SSPB. The zinc grain boundaries could be clearly observed after etching. Figure 4 (B) shows that some aggregated silica nanoparticles, which could be distinguished from the zinc grains by their different contrast, were embedded in the zinc coating formed at 5% silica sol content. However, the EDS analyses also shows the distribution of the silica phase was not uniform. As shown in Figure 4 (C), the agglomeration of the embedded silica nanoparticles decreased when the silica sol

content was increased to 15%, and the silica phase was more uniformly distributed. Figure 4 (D)

shows that when the silica sol content reached 25%, the embedded silica nanoparticles again

aggregated more strongly near to the NdFeB substrate. The relative amount of silicon also

increased in comparison with other samples. In addition to the uniformly distributed silica

nanoparticles, there existed several large-sized silica particles, which could exert a notable effect

on the zinc coating's performance. In summary, Figure 4 demonstrates that aggregation of the

silica nanoparticles embedded in the zinc coating occurred when the silica sol content in the SSPB

was either too high or too low.
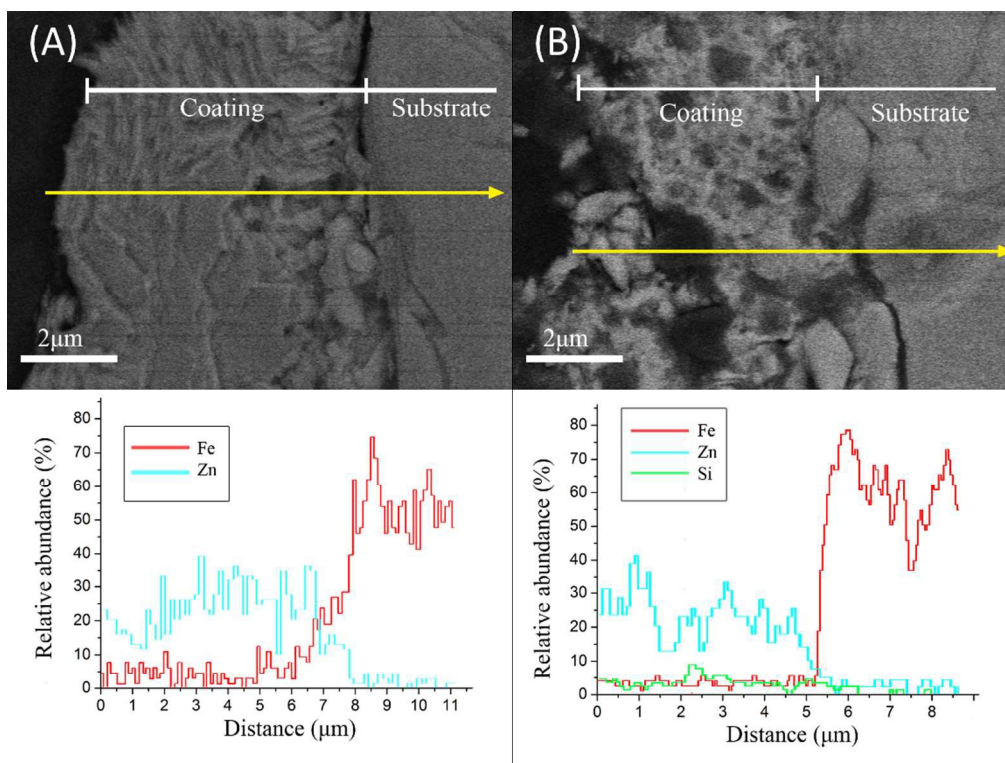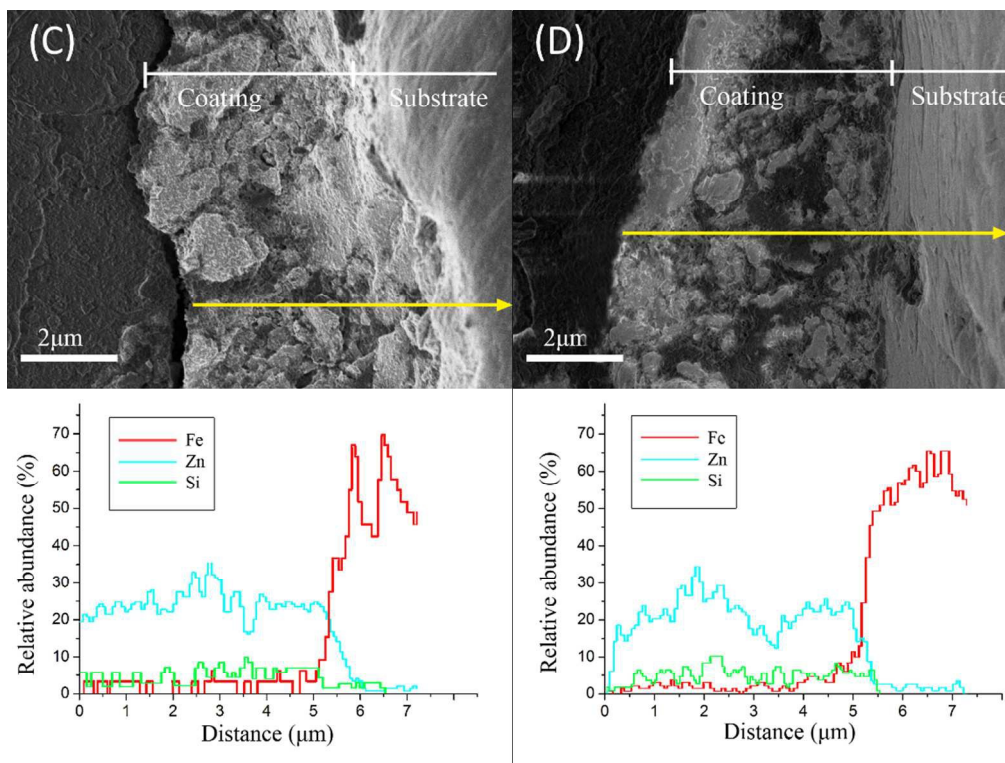
Figure 4. Cross-sectional views and EDS analyses of the zinc coatings obtained from (A) the 0% SSPB, (B) the 5% SSPB, (C) the 15% SSPB, and (D) the 25% SSPB.

To measure the effect of silica sols on the deposition process, the polarization curves of bare NdFeB cathodes were tested in plating baths with different silica sols contents. Figure 5 (A) shows the polarization curves recorded at the beginning of the electrodeposition process. From Figure 5 (A), it is apparent that the polarization curves exhibited a linear relationship at low current densities. At a fixed overpotential (η), the current density decreased with the increase in the silica sol content from 0 to 25%. The introduction of an increasing amount of silica sols led to the adsorption of more silica particles on the cathode surface. The results presented in Figure 5 (A) indicate that the adsorption of silica particles occurred at the beginning of the electrodeposition

14

process. The adsorption of more silica particles caused higher overpotential on the cathode surface.

Zeta-potential of silica particles from 5% SSPB, 15% SSPB and 25% SSPB were (-6.8±0.4) mV,

(-4.4±0.3) mV and (-3.6±0.3) mV. The silica particles may be covered by cation, like K^+ and $Zn2^+$,

and moved towards cathode under electric field. Silica particles with lower absolute value of

zeta-potential was easier to aggregate[40]. The adsorption process of silica particles was easier to

occur in 25% SSPB. So zinc coating obtained from higher silica sols content plating bath has more

adsorbed silica particles.

As shown in Figure 5 (B), when the current density increased above 2×10^{-3} A/cm^2, the

concentration polarization took on the dominant role. From the inset to Figure 5 (B), it is apparent

that the silica sols exerted a clear effect on the concentration polarization. At a fixed current

density, the cathode overpotential increased with the addition of more silica sols. The adsorbed

silica particles caused the overpotential on the cathode to rise. According to the Erdey-Gruz and

Valmer two-dimensional nucleation equation, the nucleation current density (i) and the

overpotentiality (η_k) have the following relationship:

$$\ln i = A - B\eta_k^{-1} \tag{1}$$

Where A and B are constants. There is a positive correlation between the number of crystal nuclei

and the nucleation current density. In addition to the nucleation current density, the overpotential

also affects the nucleation probability (W), as follows:

$$W = C\exp(-c/\eta_k^2) \tag{2}$$

15

where C and c are constants.
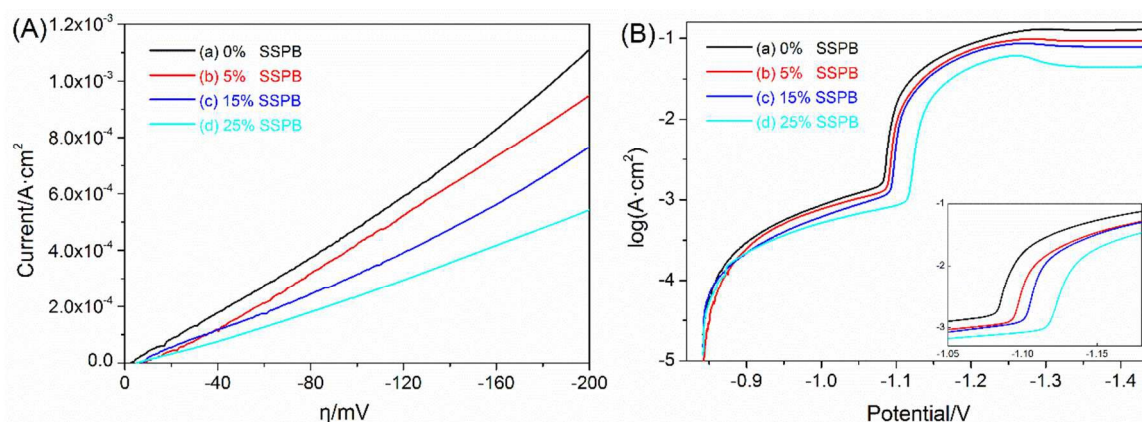
Figure 5. Polarization curves of the NdFeB cathodes in plating baths with different silica sol contents: (A) in the low current density regime and (B) the overall curves.

According to the polarization curve data shown in Figure 5 (A), when the concentration polarization is not playing the dominant role, the tested current can be regarded as the nucleation current density. The model represented by Equation (1) satisfies the hypothesis test of linearity, and it matches the data well. The results of the linear regression for $\ln i$ and η_k^{-1} are listed in Table 1. Low current density errors could be achieved for the fitted constants A and B for overpotentials below 200 mV, which indicated that the electrochemical reaction played the dominant role in the polarization effect. As shown in Figure 5 (B), when the overpotential increased above 250 mV, the role of the concentration polarization became dominant. The current density, which increased sharply with increasing overpotential, included both nucleation and concentration polarization currents. As shown in Figure 5 (B), the cathode overpotentials in different plating baths were read out for zinc coatings deposited at a current density of 1.2 A/dm^2. The fitted nucleation current

densities calculated based on the linear regression results are listed in Table 1. Because the

nucleation probability also affected the nucleation process, we assumed the nucleation probability

of the zinc coating formed in the 25% SSPB to be 0.3. Then, according to Equation (2), the other

nucleation probabilities corresponding to the 0, 5 and 15% SSPBs were 0.07, 0.11 and 0.18,

respectively. Because the nucleation current densities in the different SSPBs were similar, the

nucleation probability played the main role in determining the nucleation behavior of the zinc

coatings.[41-43] The fitted results exhibited significant differences and were well consistent with the

images in Figure 1. The adsorbed silica affected the crystallization of the zinc coatings during the

deposition process. When the zinc was electrodeposited at the same current density, zinc coatings

with higher overpotentialities tended to form more zinc grains.

Table 1. Fitted results for the electrodeposition of the zinc coatings

Silica sol content in plating bath (%)	Intercept (A)	Slope (B)	Adj. R-squared	Nucleation current density (A/cm^2)	Nucleation probability
0	-6.074	0.169	0.990	9.9×10^{-4}	0.07
5	-6.199	0.164	0.995	9.7×10^{-4}	0.11
15	-6.413	0.158	0.990	9.3×10^{-4}	0.18
25	-6.760	0.139	0.992	8.8×10^{-4}	0.3

The current efficiency for NdFeB cathode at varying SSPB is shown in Figure 6. The

increased mass was measured and converted to a current efficiency (CE) from the relation

$$CE(\%) = \frac{I_{Zn}}{I_{tot}} * 100 \qquad (3)$$

where I_{Zn} was calculated from the actual increased mass measured and I_{tot} was total current applied.

A current density of 1.2 A/dm2, which was in agreement with the previous paper, was used in the measurement. As shown in Figure 6, the current efficiency grew higher with the increase of silica sols content in the plating bath when the electrodeposition time was under 15 minutes. This may be caused by the adsorption of silica particles, which were visible in cross-section images. When the electrodeposition time was longer than 30 minutes, the current efficiency was slightly improved with the addition of silica sols. The results show that silica sols did not harm the electroplating efficiency.
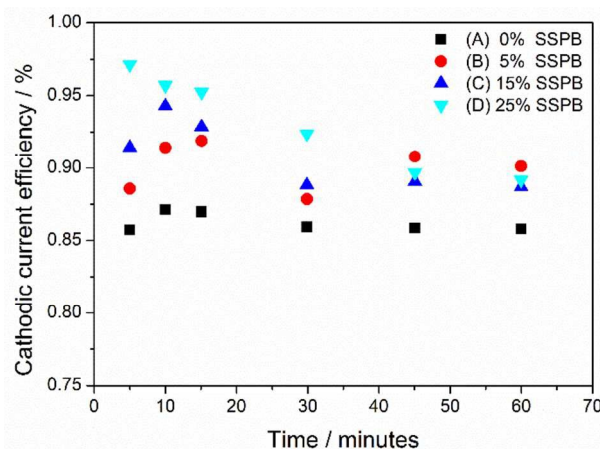
Figure 6. Current efficiency of the zinc coatings obtained from (A) the 0% SSPB, (B) the 5% SSPB, (C) the 15% SSPB, and (D) the 25% SSPB.

To evaluate the effects of the silica sol content on the zinc particles, the XRD patterns of samples prepared in the 0, 5, 15 and 25% SSPBs were recorded; the results are shown in Figure 7. All XRD pattern exhibit in common three pronounced diffraction lines, which agree with the (0 0 2), (1 0 1)

18

and (1 0 2) diffraction lines of zinc (PDF65-3358). As indicated in the XRD diagrams, the

diffraction lines varied with the increase of the silica sols content. For the coating made from 5%

SSPB (Figure 7 (b)), a stronger orientation along the (0 0 2) plane was observed in comparison

with those recorded for the zinc coating obtained from the 0% SSPB (Figure 7 (a)).[44-47] The

adsorbed silica nanoparticles at the grain boundaries may change the growth orientation of the zinc

grains. When the silica sols content continued to increase from 15% to 25% (Figure 7 (c) and

Figure 7 (d)), the relative intensities of lattice parameters were slightly changed. The change in the

X-ray diffraction intensity indicated that the silica sols modified the molecular orientation and

crystallinity of the zinc particles in the coatings. The relative intensity of (1 0 1) diffraction line

grew higher with the increase of silica sols content from 0 to 25% in plating bath. Zinc coating

with more (1 0 1) crystal orientation showed better anti-corrosion ability[48-50]. Furthermore, the

characteristic zinc diffraction line shifted rightward with the increase in the silica sol content from

0 to 15%. The diffraction line shifts of the XRD patterns may be caused by the adsorbed silica

nanoparticles between the zinc grains, which caused slight lattice distortion.[51, 52]
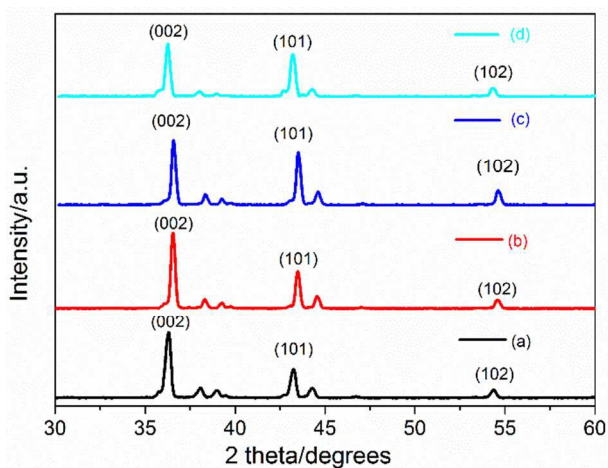
Figure 7. XRD patterns of electrodeposited zinc coatings: (a) the zinc coating obtained from the 0%

SSPB, (b) the zinc coating obtained from the 5% SSPB, (c) the zinc coating obtained from the 15%

SSPB, and (d) the zinc coating obtained from the 25% SSPB.

As shown in Figure 8, when the TEOS was hydrolyzed under acid-catalyzed conditions, part of the

Si-OC$_2$H$_5$ transformed into Si-OH. Moreover, under acidic conditions, the activity of Si-OH

groups is sufficiently high to undergo condensation under stirring. During the aging process, the –

OH groups that formed aggregated under further hydrolysis, and the silica chains formed silica

nanoparticles that were covered with –OH groups. The hydroxyl-wrapped silica nanoparticles

moved to the surface of the cathode during the electroplating process. The latter usually involves

application of cathodic potentials to the substrates, yielding cathodic reduction of

$$O_2 + 2H_2O + 4e^- \rightarrow 4OH^- \tag{4}$$

$$2H_2O + 2e^- \rightarrow 2OH^- + H_2 \tag{5}$$
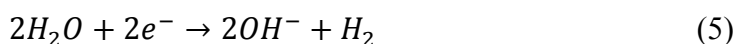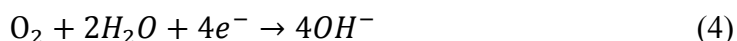
These cathodic reactions raise the pH near the conducting substrate by generating OH$^-$ ions. The

electrochemically induced OH$^-$ ions on the cathode catalyzes the condensation of silica sol to gel

on the substrate thus leads to particle formation. The intent was for the nanoparticles to become

embedded in the zinc particles to improve the physical and chemical properties of the coating.
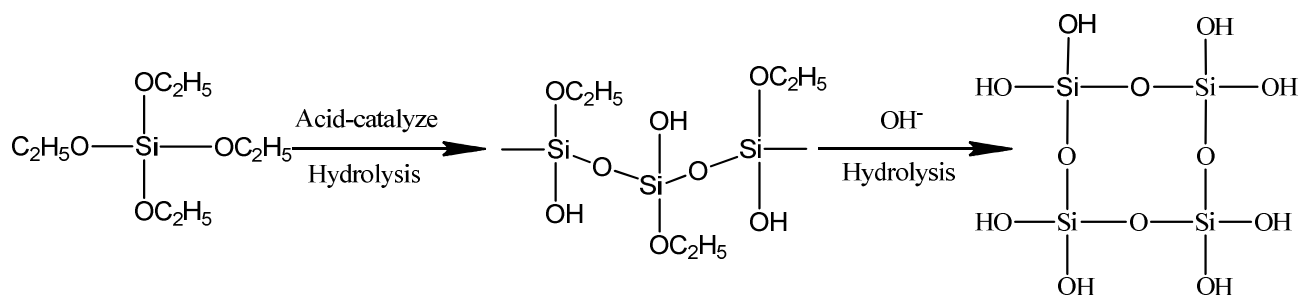
Figure 8. Growth model for silica particles under acid catalysis.

The silica sols were added to the acidic zinc plating baths, the pH of which was close to that of

the silica sol system, allowing the silica particles to remain stable in the mixture. When the electrodeposition process was performed in such a mixed plating bath, the deposition of zinc occurred. Simultaneously, the hydroxyl-rich silica sols became attached to the cathode surface due to the effect of the external electric field.[14, 23] The condensation of the silica sols on the cathode surface was promoted by the hydroxyl groups that were generated through the side reaction of the zinc electrodeposition, leading to the formation of silica nanoparticles. These silica nanoparticles could then be adsorbed onto the surfaces of the electroplated zinc particles. During the continuous zinc ion crystallization process, some of these adsorbed silica nanoparticles were covered and became embedded into zinc particles. These embedded silica nanoparticles modified the crystal characteristics and size distribution of the zinc particles.[38, 39]

In general, the uniformity of their distribution and their adsorption properties are both important to the corrosion resistance performance of zinc coatings. The standard solution with a content of 3.5 wt.% NaCl was chosen as the corrosion medium for determination and comparison of corrosion behavior in the present work. The polarization curves for the zinc-coated NdFeB substrates exposed to 3.5 wt.% NaCl solutions are shown in Figure 9 (A). Under high-overpotential conditions, the electrochemical reaction rate under kinetic control could be represented simply by the Tafel relationship. Therefore, by fitting the data via linear extrapolation at high overpotential (over 100 mV), we were able to obtain the corrosion current density (j_{corr}) from the intersection with the ordinate and the corrosion potential (E_{corr}) from the intersection with the abscissa. The E_{corr} values and j_{corr} values of the coatings formed at different silica sol contents

are listed in Table 2. Compared with the zinc coating obtained from the 0% SSPB, it is notable that

the E_{corr} of zinc coating from15% SSPB and 25% SSPB was shifted to more positive potentials:

approximately 36 mV and 40 mV, respectively. Given that E_{corr} is the measure of corrosion

susceptibility and independent on the geometry of the sample, the shift in E_{corr} to more positive

direction, suggesting an increase in corrosion resistance due to the presence of silica particles in

zinc coating. The j_{corr} value of the zinc coating obtained from the 0% SSPB was distinctly higher

than those of the coatings formed in the other baths. In the aqueous NaCl solution, the Nd-rich

phase dissolved first in the anode reaction (Equations (6) and (7)), which most likely produced a

passivation film between the substrate and the coating, thereby decreasing the corrosion rate.

Simultaneously, the zinc could dissolve to form another passivation film on the surface of the

coating (Equation (8)).[8] Nevertheless, the aggressive Cl⁻ could migrate to the interface to destroy

the passivation film thus formed, thereby accelerating the dissolution of the NdFeB. However, the

anodic current density of the zinc coating obtained from the 15% SSPB was more than one order of

magnitude lower than that of the zinc coating obtained from the 0% SSPB. This suggests that the

zinc coatings that were deposited onto the NdFeB from the SSPBs remarkably decreased the

dissolution of the NdFeB. The decrease in the current density was likely caused by the embedding

with silica nanoparticles, which filled the gaps between zinc particles. The j_{corr} values of the

coatings decreased as the silica sol content was increased from 0 to 15%. However, when the silica

sol content reached 25%, the corrosion rate of the zinc coating again increased because the

aggregation silica particles, leading to a decline in the filling effect.

$$Nd \rightarrow Nd^{3+} + 3e \tag{6}$$

$$Nd^{3+} + 3OH^- \rightarrow Nd(OH)_3 \tag{7}$$

$$Zn \rightarrow Zn^{2+} + 2e \tag{8}$$

Table 2. Electrochemical parameters derived from the polarization curves of the NdFeB-based

zinc coatings in 3.5 wt.% NaCl solutions

Silica sol content in plating bath (%)	E_{corr} (mV, vs. SCE)	j_{corr} (A/cm^2)
0	-1148	6.3×10^{-6}
5	-1158	3.2×10^{-6}
15	-1112	4.0×10^{-7}
25	-1108	7.9×10^{-7}

Comparisons of the EIS data acquired for the zinc coatings formed in different SSPBs are shown

in Figures 9 (B) and (D). These tests were also performed in neutral 3.5 wt.% NaCl solutions. In

Figure 9 (B) and (D), the experimental data were marked as points and the fitted impedance data

obtained using the proposed electrical equivalent circuit (EEC) as continuous lines. The arc curves

indicate that the electron transfer process was inhibited on the electrode surface. Furthermore, a

larger radius of the arc indicates a higher anti-corrosion resistance and a greater difficulty of

23

electron transfer. The shape of the Nyquist plots (Figure 9 (B)) for samples with different silica sol

contents indicates that the anti-corrosive property of the coatings was notably improved due to the

tightly embedded silica nanoparticles when the silica sol content in the plating bath was 15%. A

more detailed interpretation of the EIS measurement was performed by fitting the experimental

plots using the EEC depicted in Figure 9 (C). In Figure 9 (C), R_s, R_{cor}, R_{ct} are the solution

resistance, the resistance of the corrosion product and the charge transfer resistance to the ionic

current through the defects in the zinc film. CPE_1 and CPE_2 are the constant phase elements that

represent the corrosion product capacitance and double-layer capacitance due to the roughness and

inhomogeneity of the electrode surface, respectively. The CPE impedance is given by the

following equation:

$$Z_{CPE}(\omega) = Y_0^{-1}(j\omega)^{-n} \tag{9}$$

Where Y_0 is a constant that is independent of frequency, ω is the angular frequency, $j=\sqrt{-1}$, and n

is the exponential index that represents the dispersion of relaxation. W is the Warburg impedance

that represents the diffusion-controlled process at low frequencies and is attributed to mass transfer

limitations through the pits on the zinc coating.[2, 3, 11] The values of the main EEC parameters for

the different samples are presented in Table 3. All of the standard deviation values (SDV) were less

than 1% in value, which means the equivalent circuit used for fitting ac impedance data was

appropriate. As shown in Table 3, the zinc coating obtained from the 15% SSPB had an R_{ct} value of

8850 Ω cm^2, which was significantly higher than the others, implying superior anti-corrosive

properties.

Table 3. EEC parameters for the different samples

Silica sol content in plating bath (%)	R_s (Ω cm^2)	CPE_1 (Ω^{-1} cm^{-2} s^{-n})	n	R_{cor} (Ω cm^2)	CPE_2 (Ω^{-1} cm^{-2} s^{-n})	n	R_{ct} (Ω cm^2)	W (Ω^{-1} cm^{-2} s$^{-0.5}$)	SDV
0	1.2	9.6×10^{-6}	1	38.4	2.6×10^{-3}	0.89	238	1.9×10^{-2}	9.6×10^{-3}
5	1.2	6.0×10^{-6}	1	47.3	2.1×10^{-4}	0.86	616	3.6×10^{-2}	6.2×10^{-3}
15	1.2	5.1×10^{-6}	1	211.6	9.1×10^{-5}	0.92	8850	5.2×10^{-2}	6.9×10^{-3}
25	1.3	9.9×10^{-6}	1	310.8	7.8×10^{-5}	0.91	5688	7.3×10^{-2}	8.3×10^{-3}

Figure 9 (D) shows the Bode magnitude plots of the coatings formed in different SSPBs. At low frequency regions, the impedance values of the zinc-coated NdFeB samples prepared in the plating baths with non-zero silica sol contents were increased by approximately one order of magnitude compared with that of the zinc-coated NdFeB sample prepared in the 0% SSPB. At intermediate frequencies, |Z| displayed the effects of the double-layer capacitance of the interface. The |Z| behavior of the zinc coatings formed in the presence of silica sols resembled that of the zinc coating obtained from the 0% SSPB because both surfaces favored the collection of charges in a similar manner. Additionally, Figures 8 (B) and (D) show that the anti-corrosive properties of the coatings initially increased and then decreased as the silica sol content was increased from 0 to

25%, with the best performance achieved at 15% silica sol content by volume. This finding is also consistent with the results from the polarization curves. Moreover, at high frequencies, the |Z| behavior demonstrated the resistance of the protective coatings; specifically, the zinc coatings formed in the presence of silica sols had higher |Z| values compared with the zinc coating formed on the sample coated in the 0% SSPB. This change in resistance can be attributed to the electrical surface resistance of the silica particles. Because a larger |Z| value implies a lower susceptibility to corrosion, the EIS behaviors indicated that the zinc coatings formed in the presence of silica sols were most resistant to corrosion when the silica particles uniformly distributed in the coatings. The EIS results further illustrated that the silica sols were acting primarily as inhibitors of the anodic reaction (ionic barriers) for the NdFeB. The dominant feature of the decrease in the corrosion rate was the reduction in the kinetics of metallic ionization.
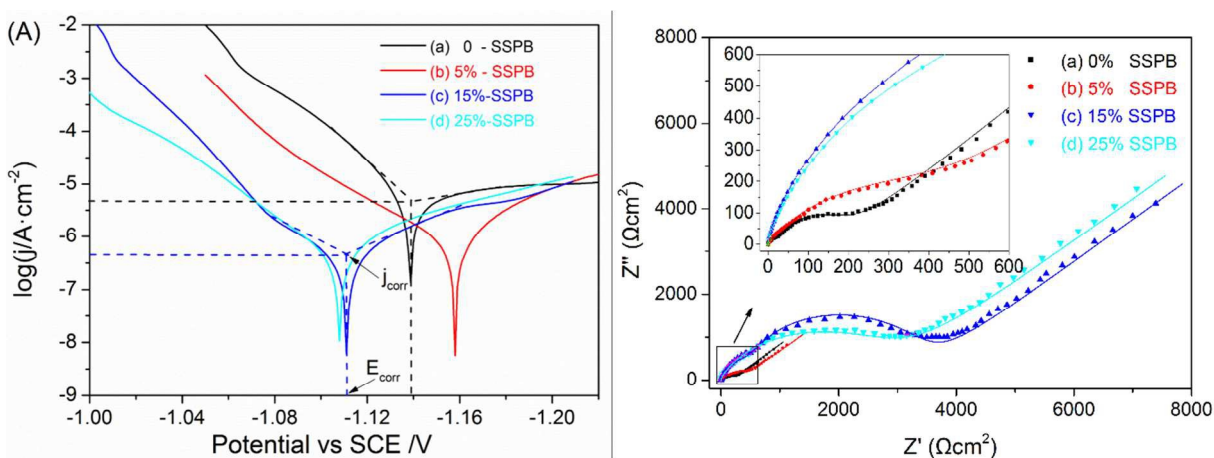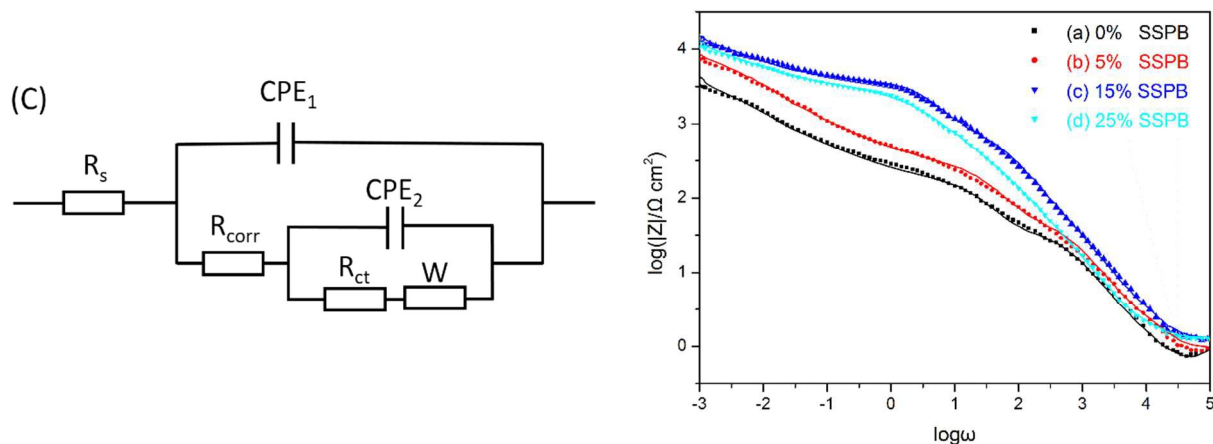
Figure 9. (A) Tafel plots, (B) Nyquist plots, (C) equivalent electric circuit and (D) Bode plots for (a) the zinc coating obtained from the 0% SSPB, (b) the zinc coating obtained from the 5% SSPB, (c) the zinc coating obtained from the 15% SSPB, and (d) the zinc coating obtained from the 25% SSPB on the NdFeB magnets.

4. CONCLUSION

Zinc coatings were obtained via electroplating from plating baths containing different silica sol contents. The morphological characteristics and corrosion resistance of the zinc coatings were influenced by the variation in the silica sol content. Moreover, the size and distribution of the silica nanoparticles embedded in the zinc particles also varied considerably. As observed from SEM images, the distributions of the embedded silica particles were most uniform when the content of silica sols in the plating bath was 15% by volume. The XRD patterns of the different coatings showed that the crystallization characteristics of the zinc coatings were also affected by the addition of silica sols. The results of electrochemical tests revealed that in comparison with the

zinc coating obtained from a silica-sol-free plating bath, the zinc coatings formed in the presence of silica sols were able to provide a more effective protective barrier for the sintered NdFeB magnets in corrosive environments. The improvement in corrosion resistance of the zinc coatings arises from two effects of the silica particles: (i) as inert and insulating materials, the silica particles protect the zinc matrix against corrosion attack, essentially forming a localized barrier film and (ii) the incorporated silica particles could also support corrosion products and slow down subsequent corrosion. The controlled crystal orientation, better uniformity and doped silica particles, which were caused by the addition of silica sols, contributed to the improvement of protection ability together.

These results demonstrate that zinc coatings that contain silica nanoparticles are a promising new means of providing corrosion protection for sintered NdFeB. Additionally, the described method is an effective way to prepare other types of silica-sol-containing metal layers formed in situ. The deposition of highly uniform and compact zinc coatings from sol-containing plating baths may also provide an effective means of protecting various other metallic surfaces.

REFERENCES

1. E. Isotahdon, E. Huttunen-Saarivirta, V. T. Kuokkala, M. Paju and L. Frisk, *Journal of Alloys and Compounds*, 2014, 585, 203-213.

2. F. Liu, Q. Li, X. K. Yang, Y. Dai, F. Luo, S. Y. Wang and H. X. Zhang, *Materials and Corrosion*, 2011, 62, 1141-1148.

3. S. Mao, H. Yang, Z. Song, J. Li, H. Ying and K. Sun, *Corrosion Science*, 2011, 53, 1887-1894.

4. X.-k. Yang, Q. Li, J.-y. Hu, X.-k. Zhong and S.-y. Zhang, *Journal of Applied Electrochemistry*, 2009, 40, 39-47.

5. K. Majima, S. Sunada, H. Ito and Y. Kaneko, *Journal of Alloys and Compounds*, 2006, 408-412, 1426-1428.

6. X. K. Yang, Q. Li, S. Y. Zhang, X. K. Zhong, Y. Dai and F. Luo, *Materials and Corrosion*, 2009, 61, 618-625.

7. H. Zhang, Y. W. Song and Z. L. Song, *Materials and Corrosion*, 2008, 59, 324-328.

8. W. He, L. Zhu, H. Chen, H. Nan, W. Li, H. Liu and Y. Wang, *Applied Surface Science*, 2013, 279, 416-423.

9. J. Zhang, C. X. Sun, Z. H. Yu, J. B. Cheng, W. Z. Li and J. Z. Duan, *International Journal of Electrochemical Science*, 2014, 9, 5712-5721.

10. M. Musiani, *Electrochimica Acta*, 2000, 45, 3397-3402.

11. S. M. Tamborim Takeuchi, D. S. Azambuja, A. M. Saliba-Silva and I. Costa, *Surface and Coatings Technology*, 2006, 200, 6826-6831.

12. S. Zheng and J. Li, *Journal of Sol-Gel Science and Technology*, 2010, 54, 174-187.

13. Z. F. Lin, D. Zhang, Y. Wang and P. Wang, *Materials and Corrosion*, 2012, 63, 416-420.

14. A. Hovestad, R. J. C. H. L. Heesen and L. J. J. Janssen, *Journal of Applied Electrochemistry*, 1999, 29, 331-338.

15. J. Chen, Y. Liu, B. Chi, J. Pu and J. Li, *Journal of Power Sources*, 2014, 256, 312-318.

16. K. Kotti and C. Kiparissides, *Macromolecular Reaction Engineering*, 2010, 4, 347-357.

17.   L.-K. Wu, X.-F. Zhang and J.-M. Hu, *Corrosion Science*, 2014, 85, 482-487.

18.   M. L. Zheludkevich, I. M. Salvado and M. G. S. Ferreira, *Journal of Materials Chemistry*, 2005, 15, 5099.

19.   S. Dalbin, G. Maurin, R. P. Nogueira, J. Persello and N. Pommier, *Surface and Coatings Technology*, 2005, 194, 363-371.

20.   X.-X. Zhang, B.-B. Xia, H.-P. Ye, Y.-L. Zhang, B. Xiao, L.-H. Yan, H.-B. Lv and B. Jiang, *Journal of Materials Chemistry*, 2012, 22, 13132.

21.   A. E. Raevskaya, Y. V. Panasiuk, O. L. Stroyuk, S. Y. Kuchmiy, V. M. Dzhagan, A. G. Milekhin, N. A. Yeryukov, L. A. Sveshnikova, E. E. Rodyakina, V. F. Plyusnin and D. R. T. Zahn, *RSC Adv.*, 2014, 4, 63393-63401.

22.   Y. Y. Fan, Y. J. Zhang and P. Dong, in *Multi-Functional Materials and Structures Ii, Pts 1 and 2*, eds. Y. S. Yin and X. Wang, Trans Tech Publications Ltd, Stafa-Zurich, 2009, vol. 79-82, pp. 1903-1906.

23.   H. Yuan, J. Wang and J. Chen, *Corrosion Engineering, Science and Technology*, 2014, 49, 197-203.

24.   E. Vanea, C. Moraru, A. Vulpoi, S. Cavalu and V. Simon, *Journal of biomaterials applications*, 2014, 28, 1190-1199.

25.   L.-K. Wu, J.-T. Zhang, J.-M. Hu and J.-Q. Zhang, *Corrosion Science*, 2012, 56, 58-66.

26.   R. Anedda, C. Cannas, A. Musinu, G. Pinna, G. Piccaluga and M. Casu, *J. Nanopart. Res.*, 2008, 10, 107-120.

27.   C. Zhu and M. J. Panzer, *ACS applied materials & interfaces*, 2015, 7, 5624-5628.

28.   W. Widiyastuti, I. Maula, T. Nurtono, F. Taufany, S. Machmudah, S. Winardi and C. Panatarani, *Chemical Engineering Journal*, 2014, 254, 252-258.

29.   N. C. López Zeballos, M. C. García Vior, J. Awruch and L. E. Dicelio, *Dyes and Pigments*, 2015, 113, 145-150.

30.   M. Azizi, W. Schneider and W. Plieth, *Journal of Solid State Electrochemistry*, 2005, 9, 429-437.

31.   C.-X. Zhao and A. P. J. Middelberg, *RSC Advances*, 2013, 3, 21227.

32.   D. D. Lovingood, J. R. Owens, M. Seeber, K. G. Kornev and I. Luzinov, *ACS applied materials & interfaces*, 2012, 4, 6875-6883.

33.   S. Cai, Y. Zhang, H. Zhang, H. Yan, H. Lv and B. Jiang, *ACS applied materials & interfaces*, 2014, 6, 11470-11475.

34.   A. Tarat, R. Majithia, R. A. Brown, M. W. Penny, K. E. Meissner and T.G.G.Maffeis, *Surface Science*, 2012, 606, 715-721.

35.   J. Du, R. Zhao, S. Chen, H. Wang, J. Li and Z. Zhu, *ACS applied materials & interfaces*, 2015, 7, 5870-5878.

36.   O. Kammona, K. Kotti, C. Kiparissides, J. P. Celis and J. Fransaer, *Electrochimica Acta*, 2009, 54, 2450-2457.

37.   A. Pepe, M. Aparicio, S. Ceré and A. Durán, *Materials Letters*, 2005, 59, 3937-3940.

38.   M. Tamilselvi, P. Kamaraj, M. Arthanareeswari and S. Devikala, *Applied Surface Science*, 2015, 327, 218-225.

39.   J. D. Brassard, D. K. Sarkar, J. Perron, A. Audibert-Hayet and D. Melot, *J Colloid Interface Sci*, 2015, 447, 240-247.

40.   M. Ramezani, M. R. Vaezi and A. Kazemzadeh, *Applied Surface Science*, 2014, 317, 147-153.

41.   M. Romero, M. A. del Valle, R. del Rio, F. R. Diaz, F. Armijo and E. A. Dalchiele, *Journal of The Electrochemical Society*, 2013, 160, G125-G134.

42.   O. Gladysz and P. Los, *Electrochimica Acta*, 2008, 54, 801-807.

43.   M. Rezaei, S. H. Tabaian and D. F. Haghshenas, *Journal of Materials Chemistry A*, 2014, 2, 4588.

44.   G. Piga, A. Santos-Cubedo, S. Moya Solà, A. Brunetti, A. Malgosa and S. Enzo, *Journal of Archaeological Science*, 2009, 36, 1857-1868.

45.   A. Nakata, H. Murayama, K. Fukuda, T. Yamane, H. Arai, T. Hirai, Y. Uchimoto, J.-i. Yamaki and Z. Ogumi, *Electrochimica Acta*, 2015, 166, 82-87.

46.   V. S. K. Valiveti, F. Singh, S. Ojha and D. Kanjilal, *Applied Surface Science*, 2014, 317, 1075-1079.

47.   M. Ashuri, F. Moztarzadeh, N. Nezafati, A. Ansari Hamedani and M. Tahriri, *Materials Science and Engineering: C*, 2012, 32, 2330-2339.

48.   L. E. Morón, A. Méndez, F. Castañeda, J. G. Flores, L. Ortiz-Frade, Y. Meas and G. Trejo, *Surface and Coatings Technology*, 2011, 205, 4985-4992.

49.   C. Cachet, F. Ganne, S. Joiret, G. Maurin, J. Petitjean, V. Vivier and R. Wiart, *Electrochimica Acta*, 2002, 47, 3409-3422.

50.   H. Jianping, L. Xinyi and L. Shunlin, *Chinese Rare Earths*, 2003, 24, 24-27.

51.   T. Sawabe, M. Akiyoshi, K. Yoshida and T. Yano, *Journal of Nuclear Materials*, 2011, 417, 430-434.

52.   K. Meena, K. Muthu, V. Meenatchi, M. Rajasekar, A. Aditya Prasad and S. Meenakshisundaram, *Spectrochimica acta. Part A, Molecular and biomolecular spectroscopy*, 2014, 125, 308-312.

395x101mm (150 x 150 DPI)